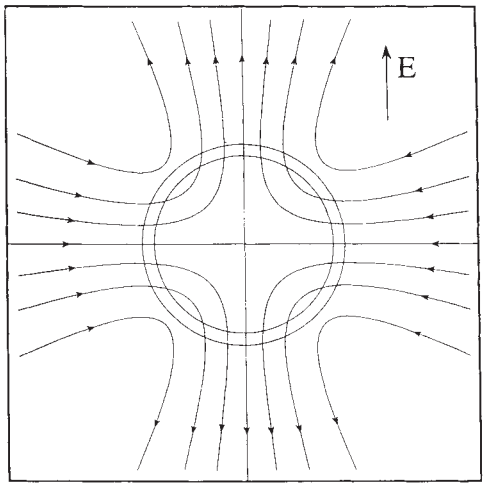


FIG. 3 Streamline pattern for flow engendered by a circular-shaped cloud of dispersion immersed in a clear fluid with a lower conductivity and dielectric constant, calculated from the model described in the text.

forces can be described in terms of Maxwell's stress tensor or as a body force[15,16], that is,

$$\mathbf{f}_e = -\tfrac{1}{2}\varepsilon_0 \mathbf{E}\cdot\mathbf{E}\nabla\varepsilon + \rho_e \mathbf{E}$$

where $\mathbf{f}_e$ is the electric body force per unit volume, $\varepsilon_0$ is the permittivity of free space, $\mathbf{E}$ is the electric field strength, $\nabla\varepsilon$ is the gradient of the local dielectric constant, and $\rho_e$ is the free charge per unit volume. Gradations in the dielectric constant arise from the factors mentioned earlier. Free charge stems from the polarizing action of the applied field on ions that carry the current. To calculate the flow field arising from the action of these electrical body forces, the Stokes equations must be solved; clearly, one must know how the dielectric constant, charge and electric field are distributed to do this[8,17]. In our calculation, we take account of effects due to the polarization force and the force engendered by free charge created by the action of the imposed field in regions where the dielectric constant and conductivity vary smoothly. Accordingly, in addition to the Stokes equations, we employ equations for transport of charge along with the relation between charge and potential, and solve for the flow field numerically.

A qualitative picture of the flow patterns can be obtained from a simple model where the dielectric constant and conductivity distributions are prescribed. This was done for situations where a transverse electric field acts on a circular region with dielectric constant $\varepsilon_1$ and conductivity $\sigma_1$, surrounded by a region with properties $\sigma_2$ and $\varepsilon_2$; each property varies smoothly in the (thin) transition zone. Figure 3 depicts the situation and shows the streamlines of the velocity field calculated when the dielectric constant and conductivity of the interior exceed those in the exterior. In this case the dispersion would be drawn out into a ribbon-like shape oriented parallel to the field. (In three dimensions the shape would be ellipsoidal.) The flow direction reverses when the conductivity of the interior is less than that of the exterior, and the sample takes up a flat configuration orthogonal to the field. These features are in complete agreement with our experimental observations.

The relation between the direction and strength of the flow is complicated by the large number of parameters involved. Generally, however, if the difference between the dielectric constants of the two regions is not too large, flow will be in the direction of the applied field if the interior conductivity exceeds that of the exterior. The sense of the flow reverses when the conductivities are reversed. For apolar liquids with low conductivities, electrical forces due to free charge and dielectric-constant variations each play a role.

Although the experiments presented here used $BaTiO_3$/castor oil dispersions, the technique is not restricted to this system. Indeed, provided that there exists a sufficient mismatch in conductivity and/or dielectric constant, any colloidal dispersion nested within any ambient fluid may be manipulated in a similar manner. An example is the observation of dispersion bands during protein electrophoresis. In such experiments, a fluid bolus containing protein molecules is immersed inside a buffer solution and exposed to an electric field. As the protein molecules migrate through the gel, becoming separated on the basis of charge, bands appear to grow in an orthogonal direction to the applied field. The formation of such band structures is suspected of involving electrohydrodynamic processes similar to the ones described here[8,17]. □

Received 12 September 1994; accepted 14 February 1995.

1. Lachman, I. M., Bagley, R. D. & Lewis, R. M. *Ceram. Soc. Bull.* **60,** 202–205 (1981).
2. Tummala, R. R. *et al. IBM J. Res. Dev.* **36,** 889–904 (1992).
3. Newnham, R. & Ruschau, G. R. *J. Am. Ceram. Soc.* **74,** 463–480 (1991).
4. Gast, A. P. & Zukoski, C. F. *Adv. Colloid Interface Sci.* **30,** 153–202 (1989).
5. Halsey, T. C. *Science* **258,** 761–766 (1992).
6. Zukoski, C. F. *A. Rev. Mater. Sci.* **23,** 45–78 (1993).
7. Rosensweig, R. E. *Ferrohydrodynamics* (Cambridge Univ. Press, New York, 1985).
8. Rhodes, P. H., Snyder, R. S. & Roberts, G. O. *J. Colloid Interface Sci.* **129,** 78–90 (1989).
9. Randall, C. A., Miyazaki, S., More, K. L., Bhalla, A. S. & Newnham, R. E. *Mater. Lett.* **15,** 26–30 (1992).
10. Dogan, F., Liu, J., Sarikaya, M. & Aksay, I. A. in *Proc. A. Meeting EMSA* Vol. 50 (ed. Bailey, G. W.) 304–305 (San Francisco Press, San Francisco, 1992).
11. Kingery, W. D., Bowen, H. K. & Uhlmann, D. R. *Introduction to Ceramics* (Wiley, New York, 1976).
12. Scott, J. F. & Paz de Araujo, C. A. *Science* **246,** 1400–1405 (1989).
13. Glass, A. M. *Mater. Res. Soc. Bull.* **13,** 16–20 (1988).
14. Hirata, Y. & Kawabata, M. *Mater. Lett.* **16,** 175–180 (1993).
15. Landau, D. & Lifshitz, E. M. *Electrodynamics of Continuous Media* (Pergamon, New York, 1960).
16. Russel, W. B., Saville, D. A. & Schowalter, W. R. *Colloidal Dispersions* (Cambridge Univ. Press, 1989).
17. Saville, D. A. *Phys. Rev. Lett.* **71,** 2907–2910 (1993).

ACKNOWLEDGEMENTS. We thank F. Dogan for processing the barium titanate powder. Partial support for M.T. was provided by the Fulbright Commission. This work was supported by the US Air Force Office of Scientific Research, and the Microgravity Science and Applications Division of NASA.

# Silica aerogel films prepared at ambient pressure by using surface derivatization to induce reversible drying shrinkage

**Sai S. Prakash*, C. Jeffrey Brinker*†‡, Alan J. Hurd§ & Sudeep M. Rao***

* University of New Mexico/Sandia National Laboratories Advanced Materials Laboratory, 1001 University Boulevard SE, Albuquerque, New Mexico 87106, USA
† Ceramic Synthesis and Inorganic Chemistry Department 1846,
§ Ceramic Processing Science Department 1841,
Sandia National Laboratories, Albuquerque, New Mexico 87185, USA

**HIGHLY porous inorganic films have potential applications as dielectric materials, reflective and anti-reflective coatings, flat-panel displays, sensors, catalyst supports and super-insulating architectural glazings[1–3]. Aerogels[4] are the most highly porous solids known, and can now be prepared from inorganic[5] and organic[6,7] precursors with volume-fraction porosities of up to 99.9% (ref. 8). Aerogels are normally prepared by supercritical extraction of the pore fluid from a wet gel[1], which prevents the network collapse that is otherwise induced by capillary forces. But supercritical processing is expensive, hazardous and incompatible with the processing requirements of many potential applications,**

‡ To whom correspondence should be addressed.

**thus severely restricting the commercial exploitation of aerogels. Here we describe a means of preparing aerogels by a simple dip-coating method at ambient pressure without the need for supercritical extraction. We add surface groups to the inorganic gel which make drying shrinkage reversible[9]: as the solvent is withdrawn, the gel springs back to a porous state. We can generate aerogel films with 98.5% porosity using this approach. We anticipate that it will greatly expand the commercial applications of these materials.**

During conventional sol–gel film deposition by dip-coating, an entrained inorganic sol is concentrated on a substrate surface by evaporation leading to aggregation and the formation of a physical or chemical gel (Fig. 1)[10]. Continued evaporation creates liquid–vapour menisci, which, for wetting fluids, causes the liquid to be in tension[11]. This tensile stress in the liquid cause, in turn, shrinkage (compressive stress on the solid phase) accompanied by continued polymerization of the gel network, resulting normally in irreversible drying shrinkage (the film remains in its most compacted state) and limiting the film porosity to the approximate range 10–60%. Supercritical drying eliminates liquid–vapour interfaces and thus capillary tension-induced shrinkage, but it is not compatible with liquid-to-solid coating operations, such as sol–gel, that rely on evaporation for coating solidification; nor is it suitable for continuous operations such as dip-coating.

An alternative means of preserving the porous network of the wet gel state is to establish processing conditions[12] whereby drying shrinkage is reversible (Fig. 1). Such conditions are achieved when the hydroxylated surface of the inorganic gel is derivatized with organosilanes via standard silylation routes[13]. Organosilyl-terminated surfaces do not participate in condensation reactions or hydrogen bonding as the gel is collapsed by the capillary tension developed during drying. Therefore as the liquid–vapour menisci recede into the gel interior and any remaining liquid is in a pendular state, the shrunken elastic network progressively 'springs back' toward its original porous state. It is this principle that we have now successfully demonstrated.

We prepared organosilyl derivatized silica (DS) sols from tetraethoxysilane (TEOS) and trimethylchlorosilane (TMCS) according to the following procedure: TEOS diluted in ethanol was partially hydrolysed with water under acidic conditions at 60 °C (molar ratios TEOS:ethanol:$H_2O$:HCl = 1:3.8:1.1:7 × $10^{-4}$). After 90 min of stirring, aqueous ammonium hydroxide was added with ethanol at room temperature resulting in the

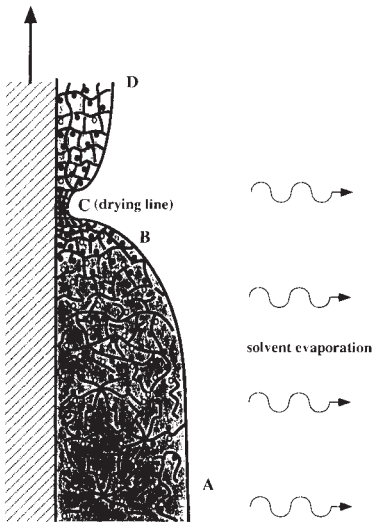


FIG. 1 Schematic diagram of steady-state film thickness profile (the dynamic film profile remains steady relative to the inertial lab frame) showing successive stages of structural evolution of aerogel film with evaporation of pore fluid during dip-coating at constant withdrawal rate. Filled circles, unreactive organosilyl-terminated surface sites; open circles, reactive surface silanol (hydroxyl) groups. Region A–B is the pre-gelation stage: the inorganic sol (colloidal dispersion of polymers or particles in a liquid) is concentrated by evaporation promoting further polymerization via condensation reactions between silanol groups. B is the gel point: a continuous network develops marking the appearance of finite elastic moduli. Region B–C is the initial drying stage: capillary tension $P$ ($=-2\gamma_{LV}/r_m$, where $\gamma_{LV}$ is the liquid–vapour surface tension and $r_m$ is the radius of the meniscus) develops in the pore fluid, causing shrinkage of the gel network. C is the drying line: a line (in plane parallel to the substrate surface) of maximum thickness gradient where capillary tension is maximized ($r_m$ is reduced to $r_p/\cos\theta$, where $r_p$ is the gel pore radius and $\theta$ is the wetting angle). Region C–D is the final drying stage: capillary pressure is reduced as liquid–vapour menisci recede into gel film interior and remaining liquid becomes isolated in pendular state and then is fully evaporated. Surface-derivatized sols exhibit expansion or 'spring-back' in this region because chemical cross-linking in the fully compacted state (C) is prevented by organosilyl groups, allowing drying shrinkage to be reversible.

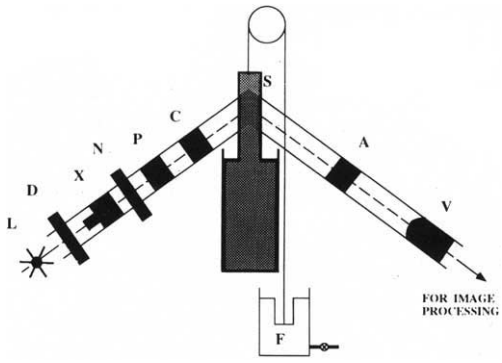


FIG. 2 *In situ* ellipsometric imaging of film deposition to observe evolution of porosity. L, He–Ne laser source ($\lambda = 6{,}328$ Å); D, depolarizer; X, beam-expander; N, diffusing screen; P, polarizer; C, compensator; S, sample; A, analyser; V, video camera; F, float (PCSA arrangement).
METHODS: An ~1-cm-diameter spot of polarized light was used to illuminate the steady-state depositing film near the drying line, incident at 67.5°. The polarization change on interaction with the drying film was analysed from the video-recorded images to quantify independently refractive-index and film-thickness profiles. Before quantitative analysis, qualitative information was inferred by observing the interference-fringe characteristics on the TV monitor. Gradients in film thickness and/or refractive index give rise to interference fringes; the closer the fringes, the steeper the gradient. Also, the relative movement of fringes indicates the direction of the gradient. Film-thickness and refractive-index profiles were obtained using the photometric detection method[22], which involves the measurement of light intensity profiles from the recorded images. At any point $x$, on the steady-state profile, intensity ($I$) depends on the ellipsometric parameters $\Psi$ and $\Delta$ (film characteristics), the settings of the optical elements (polarization characteristics) and the optical constants of the apparatus (such as source intensity and the ideality of the elements). With the polarizer angle ($P$) set at 0° and the compensator ($C$) at 45°, the polarization change on interaction with the forming film was analysed at various positions of the analyser ($A$). For $P = 0°$, $C = 45°$, intensity is given by $I = 2C_1\,[\tan^2\Psi + (1-\tan^2\Psi)\sin^2 A + \tan\Psi \sin\Delta \sin 2A]$, where $C_1$ is a parameter independent of $P$, $C$ and $A$. The linear region of the sinusoidal $I$ versus $A$ curve was chosen suitably, and the position-dependent intensity data $I(x)$ were obtained for $A = -90°$, $-120°$ and $-135°$. These profiles were used to obtain $\Psi(x)$ and $\Delta(x)$ profiles by eliminating $C_1$, and were then converted into refractive-index $n(x)$ and thickness $h(x)$ profiles using standard ellipsometric equations and plots. In plotting the film-thickness profile, the true thickness was deduced as the sum of the calculated first phase thickness (from $\Psi$ and $\Delta$) and the fringe number times the phase thickness multiple, that is $h$ = calculated thickness + (fringe number × phase thickness). For the ellipsometric imaging experiments, hexane was replaced with ethanol, due to the latter's lower volatility. (This replacement does not affect the sol-chemistry significantly, as determined using $^{29}$Si NMR). Image analysis was performed using Image 1.49 VDM (W. Rasband, NIH) and Screenplay II software (SuperMac Technology, Inc, Sunnyvale, California).

final molar ratios TEOS:ethanol:$H_2O$:HCl:$NH_4OH$ = 1:38.8:3.6:$7\times10^{-4}$:$2\times10^{-3}$. Following gelation and ageing at 50 °C, the gel was washed in ethanol, followed by hexane, and derivatized with TMCS in hexane. The derivatized gel (molar ratio methyl:Si = 1:1.83 determined from $^{29}$Si NMR) was diluted with hexane and sonicated for a period of 20–25 min at a power of ~95 W to create a fluid sol suitable for dip-coating.

Films were deposited on ~2-cm-wide strips of polished ⟨100⟩ Si by dip-coating at rates of 0.09–1.9 cm $s^{-1}$. Film-thickness and refractive-index profiles in an ~1-cm zone near the drying line were determined *in situ* during deposition using a broad-beam imaging ellipsometer described in Fig. 2 and ref. 14. For comparison purposes, imaging ellipsometry was also performed during deposition of a standard silica (SS) sol prepared in an

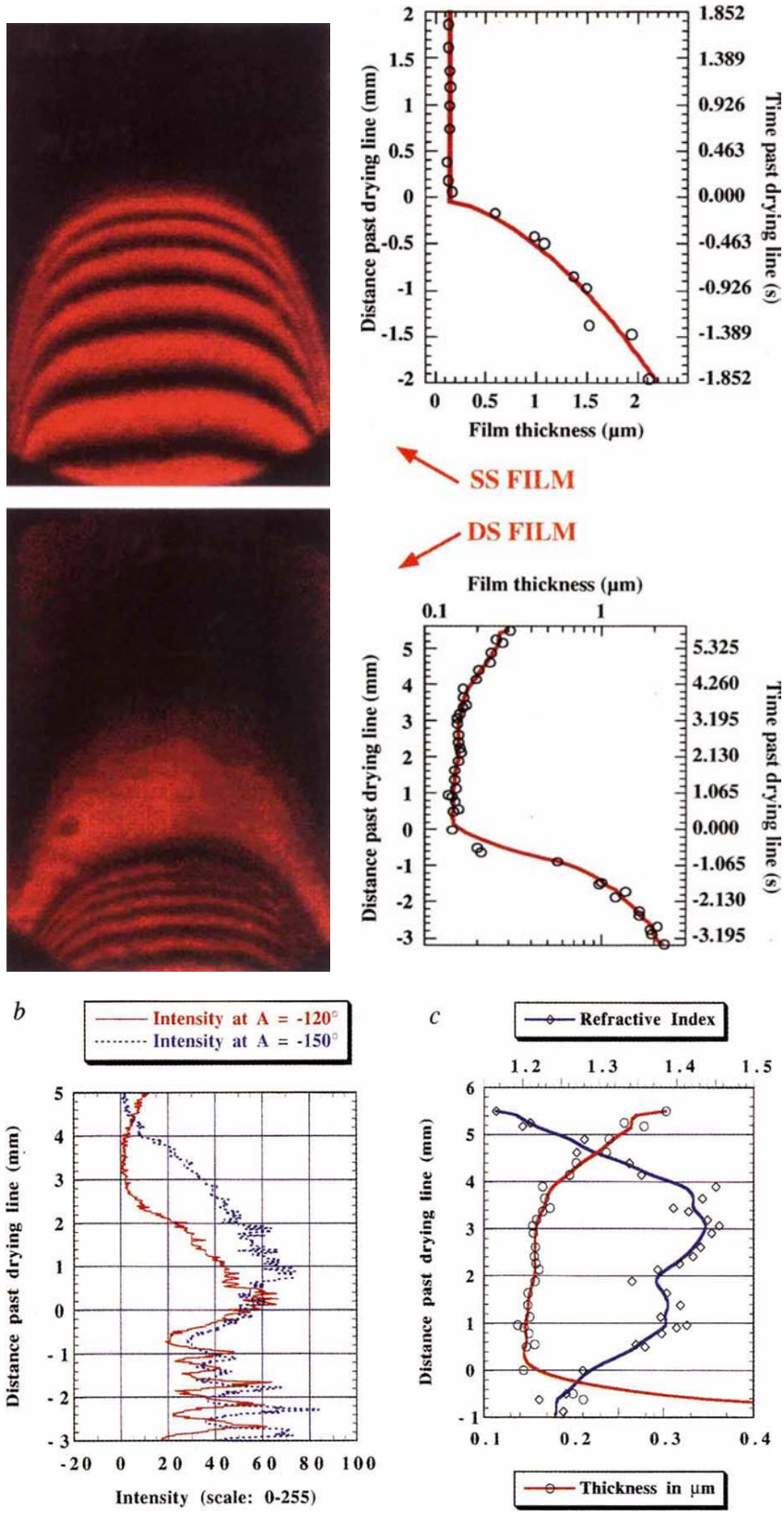


FIG. 3 *a*, Ellipsometric images of an ~1-cm zone around the drying line with corresponding thickness profile data for the SS (standard sol) and DS (derivatized sol) cases. Fringe characteristics and corresponding thickness data indicate that the SS film (top) thins approximately parabolically (exponent ~0.64) up to the drying line, and remains constant in thickness and refractive index above it (absence of fringes). The DS film (bottom), thins in comparable fashion up to the drying line, but 'springs back' above it (presence of broad fringes). The zeros on the *y*-axes correspond to the drying line. The DS film thickness profile is plotted on a semi-log scale. The change in DS film thickness on 'spring-back' is ~100%. At distances >6 mm above the drying line, the DS thickness and index remain roughly constant, indicating that the film is close to final dryness. *b*, Intensity profiles at two different *A* positions (−120°, −150°). The fringes, indicated by peaks in the plot, diverge (or equivalently converge) upon change of *A*, about the drying line. This is a consequence of the presence of a valley in film thickness in the vicinity of the drying line. As expected, the fringes in the SS film move unidirectionally. *c*, Refractive-index and thickness profiles in the 'spring-back' region.

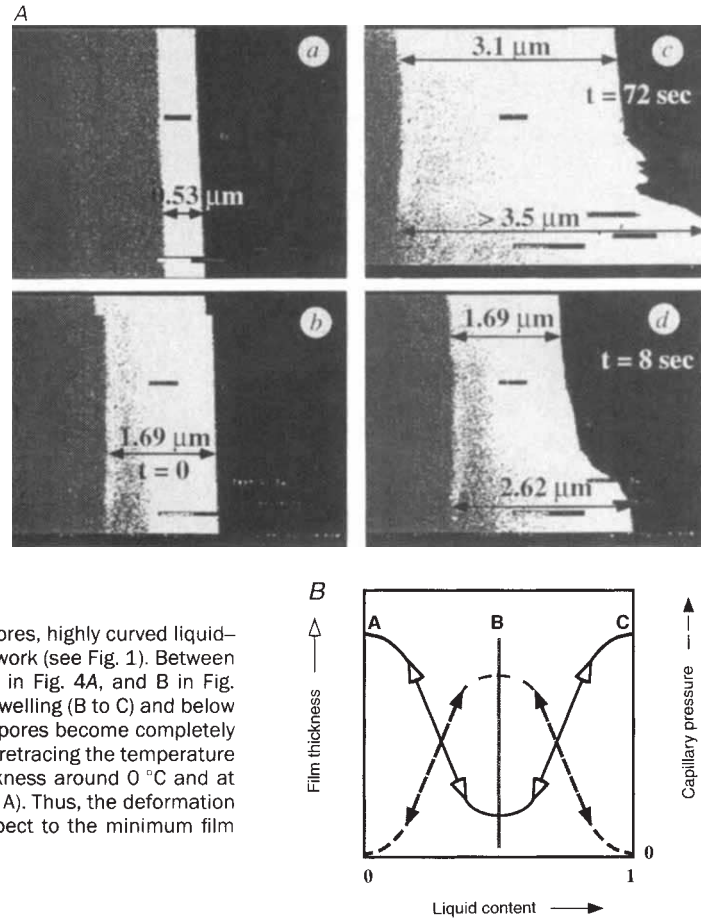


FIG. 4 *A*, Environmental scanning electron microscopy (ESEM) snapshots of an ambient-pressure aerogel film (without pyrolysis) at various stages of capillary pressure-induced deformation. Counter-clockwise from top left; *a*, film at maximum state of compaction, *b–d*, dynamic 'spring-back' with release of capillary stress in the pores on final evaporation of the solvent. As a finite scan rate (~7 s per frame) was used, every point on a frame is at a slightly later time than the point just above it. *B*, Qualitative schematic of the reversibility of deformation determined from ESEM data. 'Liquid content', the *x*-variable, is arbitrarily defined as 0 for a dry film, and 1 when the film is completely saturated with liquid (that is, when the liquid–vapour menisci in all the pores have zero curvature).
METHODS. The dry sample (~3.5 μm thick, crack-free aerogel film) was mounted on a stage and placed in the ESEM (Electroscan) chamber operating at a constant pressure of 5 torr. The temperature of the stage (and hence, the sample) was controlled between −10 and +40 °C by using an external chiller. The chamber was filled with pure *n*-butanol vapour. Vapour condensation onto, and liquid reevaporation from, the film were controlled by varying the temperature. The equilibrated thickness of the film was monitored at different temperatures, allowing observation of its dependence on capillary pressure. The process was continuously recorded on video tape. Starting from a value of ~3.5 μm (dry film thickness, A in Fig. 4*B*), the film shrank (A to B) as it was cooled to below 15 °C (cooling cycle). This was consistent with the fact that as liquid first enters the pores, highly curved liquid–vapour menisci form ($r_m \sim r_p$) exerting a compressive stress on the network (see Fig. 1). Between +4 and −3 °C, the thickness reached its minimum of ~0.53 μm (*a*) in Fig. 4*A*, and B in Fig. 4*B*). As the temperature was lowered below −3 °C, the film exhibited swelling (B to C) and below −9 °C expanded to near dry-film thickness (C). Swelling occurs as the pores become completely filled with liquid and $r_m \rightarrow \infty$ reducing the capillary pressure to zero. On retracing the temperature path (heating cycle), the film shrank steadily, reached minimum thickness around 0 °C and at ~3 °C exhibited a sudden 'spring-back' from ~1.7 to 3.5 μm (C to B to A). Thus, the deformation was almost perfectly reversible. The maximum deformation with respect to the minimum film thickness was ~600%.

identical fashion to the DS sol described above except for omission of the organosilyl derivatization step.

Figure 3*a* compares instantaneous frames of the ellipsometric images of the DS and SS films obtained in the steady coating regime along with their corresponding film-thickness profiles. The presence of fringes indicates a gradient in thickness and/or refractive index: the closer the fringe spacing, the steeper the gradient. The SS film thins with a roughly parabolic shape (thickness $h \propto$ distance $x^{0.64}$) as we have observed for titania sol–gel film deposition[15] and remains in the shrunken state above the drying line as is evident from the lack of any discernible fringes or colour changes in this region. By comparison, the DS sol thins in a manner similar to the SS sol but, above the drying line, broad fringes are observed indicative of a thickness/refractive index gradient. Figure 3*b* shows intensity profiles determined from the ellipsometric images at two different analyser settings. The movement of the intensity peaks away from (or equivalently towards) each other for different analyser settings indicates the presence of a valley in the film thickness in the vicinity of the drying line. The DS film-thickness profile (Fig. 3*a*) determined from the ellipsometric images clearly shows a gradual dilation or 'spring-back' of the film above the drying line consistent with a progressive reduction in the film volume element on which the capillary tension is exerted as the pore fluid is evaporated. Corresponding refractive-index and porosity profiles (Fig. 3*c*) show the concomitant creation of porosity within the film. Subsequent heat treatment at >450 °C in air pyrolyses the trimethylsilyl ligands causing the film porosity to exceed 90% (ref. 16).

The sequence of environmental scanning electron microscope (ESEM) images shown in Fig. 4 demonstrates that, for films prepared from DS sols (without a pyrolysis step), surface derivatization allows extraordinary, reversible capillary tension-induced strains to be achieved ($\Delta V/V > 6$, where $V$ represents the film volume in its most compact state) without cracking. Magic-angle-spinning $^{29}$Si NMR spectra show 60–70% fully condensed $Q^4$ species, ~30% $Q^3$ species, and 0–10% $Q^2$ species in the silica framework (where the superscript denotes the average number of bridging siloxane bonds surrounding the silicon nucleus under consideration), corresponding to overall extents of condensation comparable to those generally observed for brittle xerogels[17]. The manner in which a highly cross-linked inorganic network can accommodate such large strains is unclear at present, but is believed to be due to the preservation of large fractal clusters within the film[18] and the size-dependent elastic moduli of these clusters[19]. Similarly, cracking of such thick gel films (up to 3.5 μm) is presumably avoided by an unusually low film elastic modulus[20].

Factors that control the extent of surface derivatization and the film modulus control the extent of spring-back, allowing the film porosity to be tailored over wide ranges (30 to >90%)[16]. A significant implication of this research is that derivatization of electropositive metal alkoxides with multidentate ligands such as acetate, acetylacetonate, or alcohol amines (used extensively to 'cap-off' reactive terminal hydroxyl groups in the preparation of multicomponent inorganic thin films[21]) may similarly result in reversible shrinkage and lead to unwanted porosity in the deposited film. This hypothesis has been confirmed by preliminary imaging ellipsometry results performed during deposition of an acetylacetonate-derivatized titanium butoxide sol system (S.S.P., Schwartz, R. W. and C.J.B., unpublished data). Finally the extraordinary, reversible capillary tension-induced strains observed for derivatized films suggest applications as actuators, transducers and environmental sensors. □

Received 12 January; accepted 10 February 1995.

1. Fricke, J. *Scient. Am.* **256,** 68–73 (1988).
2. Vacher, R., Phalippou, J., Pelous, J. & Woignier, T. (eds) *Coll. de Phys. (Fr.)* **24,** 1–249.
3. Fricke, J. (ed.) *J. non-cryst. Solids* **145,** 1–259 (1992).

4. Kistler, S. S. *Nature* **127,** 741 (1931).
5. Fricke, J. (ed.) *Aerogels* (Springer, Berlin, 1986).
6. Pekala, R. W., Alviso, C. T., Kong, F. M. & Hulsey, S. S. *J. non-cryst. Solids* **145,** 90–98 (1992).
7. Schwertfeger, F., Glaubitt, W. & Schubert, U. *J. non-cryst. Solids* **145,** 85–89 (1992).
8. Hrubesh, L. W. *Chem. Ind.* **24,** 824–827 (1990).
9. Deshpande, R., Smith, D. M. & Brinker, C. J. *US Patent Applic.* SN PCT/US94/05105 (1992).
10. Brinker, C. J., Hurd, A. J., Schunk, P. R., Frye, G. C. & Ashley, C. S. *J. non-cryst. Solids* **147/148,** 424–436 (1992).
11. Brinker, C. J. & Scherer, G. W. *Sol-Gel Science* Ch. 8 (Academic, San Diego, 1990).
12. Smith, D. M., Deshpande, R. & Brinker, C. J. in *Better Ceramics Through Chemistry V* (eds Smith, M.-H., Klemperer, W. G. & Brinker, C. J.) 567–572 (Vol. 271, MRS Symp. Proc. Mater. Res. Soc., Pittsburgh, 1992).
13. Plueddemann, E. P. *Silane Coupling Agents* (Plenum, New York, 1991).
14. Hurd, A. J. & Brinker, C. J. *J. Phys. (France)* **49,** 1017–1025 (1988).
15. Brinker, C. J., Hurd, A. J., Frye, G. C., Ward, K. J. & Ashley, C. S. *J. non-cryst. Solids* **121,** 294–302 (1990).
16. Prakash, S. S., Brinker, C. J. & Hurd, A. J. *J. non-cryst. Solids* (submitted).
17. Brinker, C. J. & Scherer, G. W. *Sol-Gel Science* Ch. 9 (Academic, San Diego, 1990).
18. Pelous, J., Foret, M. & Vacher, R. *J. non-cryst. Solids* **145,** 63–70 (1992).
19. Ball, R. C. *Physica* D**38,** 13–15 (1989).
20. Thouless, M. D. *Acta Metall.* **36,** 3131–3135 (1988).
21. Yi, G. & Sayer, M. *Ceram. Bull.* **70,** 1173–1179 (1991).
22. Azzam, R. M. A. & Bashara, N. M. *Ellipsometry and Polarized Light* Ch. 3 (North-Holland, Amsterdam, 1987).

ACKNOWLEDGEMENTS. We thank D. Smith and D. Stein for useful discussions and D. Stuart for technical assistance. This work was supported by the US Department of Energy Basic Energy Sciences Program. Sandia National Laboratories is a US Department of Energy Facility.

# Oceanic evidence for coherent fluctuations in Fennoscandian and Laurentide ice sheets on millennium timescales

**Torben Fronval*, Eystein Jansen*, Jan Bloemendal† & Sigfus Johnsen‡§**

Jan Bloemendal† & Sigfus Johnsen‡§
* Department of Geology, University of Bergen, Allegaten 41, 5007 Bergen, Norway
† Department of Geography, University of Liverpool, Liverpool L69 3BX, UK
‡ The Niehls Bohr Institute, Department of Geophysics, University of Copenhagen, Haraldsgade 6, 2200 Copenhagen N., Denmark
§ Science Institute, Department of Geophysics, University of Iceland, Dunghaga 3, 107 Reykjavik, Iceland

**Proxy temperature records from Greenland ice cores[1,2] and North Atlantic sediment cores[3] have provided evidence for a high degree of climate instability during the last glacial period. Much of this variability seems to be linked with the dynamics of the Laurentide ice sheet that covered North America at this time[3], which discharged iceberg flotillas into the North Atlantic that are now recorded in sediment cores as Heinrich events[4]. How (if at all) this variability was manifested on the other side of the Atlantic—in the Nordic seas and the ice sheets of northwest Europe and Scandinavia—has been unclear. Here we present sediment, microfossil and oxygen isotope data from a sediment core in the Norwegian sea, which reveal cooling events and iceberg discharges analogous to Heinrich events. We show that these climate fluctuations in the Norwegian Sea were in phase, or were phase-locked, with air temperatures over Greenland, suggesting that the rapid changes in heat fluxes in the North Atlantic recorded in previous records[3] were felt in this high-latitude region. The iceberg discharges in our record seem to have come from the Fennoscandian ice sheet, implying that this and the Laurentide ice sheets fluctuated coherently on timescales shorter than those of Milankovitch orbital cycles.**

Bond *et al.*[3] correlated air temperature data from the Summit ice core with records of proxy sea surface temperature (SST) from the North Atlantic, and documented a link between changes in the behaviour of the Laurentide ice sheet (as recorded in Heinrich layers in sediment cores), atmospheric temperature and North Atlantic heat flux. The records that we present here allow us to assess how these variations in North Atlantic heat flux affect high-latitude regions of the Greenland, Iceland and Norwegian seas, and how they were coupled to the Eurasian ice sheets. We describe sediment-core records covering the period 10–60 kyr from ODP site 644 on the Vöring plateau, which we correlate with the Summit[1], DSDP site 609[3] and V23-81[3] proxy temperature records. The site was chosen because of its location in the northern limb of the North Atlantic heat conveyor and its closeness to the North European ice sheet (Fig. 1*a*). Shifts in several sedimentary parameters occur on millennium timescales at site 644. The smaller oscillations bundle into cycles, often with typical asymmetric saw-tooth shapes and sharp boundaries similar to the cooling cycles in North Atlantic sediment cores[3] and Greenland ice cores[1] (Fig. 1*b*). The number of cycles and their shape are nearly identical in the records from Greenland, the North Atlantic and the Norwegian Sea. The occurrence of a zone characterized by low foraminifera concentration and low $\delta^{18}O$ values—similar to North Atlantic Heinrich layers[3,5] at the culmination of each cooling cycle (Fig. 2)—strengthen the correlations. The five youngest of these Heinrich-type sedimentary events correlate to H1–H5 in the North Atlantic record, whereas the oldest one correlates to H6. The event between H5 and H6 has a North Atlantic correlative in a zone with low $\delta^{18}O$ values but only slightly lowered foraminifera concentrations[3,5]. A large number of the ice-core interstadials, numbered 1–16, can be identified in the Vöring plateau record, although in some cases the correlation relies on a very few data points. Between interstadials 1 and 2, one additional 'interstadial' is recognized in the Norwegian Sea record, probably corresponding to a $\delta^{18}O$ maximum without sharp boundaries in the Summit ice core. With this correlation, the cycles at site 644 can be viewed as reflections of the main stadial–interstadial cycles of the ice core and the North Atlantic cooling cycles. A complete correlation with the high-amplitude fluctuations (Dansgaard–Oeschger events) within the ice-core cooling cycles is not possible, although many of these may be recognized.

At site 644 the cycles are primarily expressed by variations in $\delta^{18}O$, foraminiferal content, magnetic susceptibility, grain size (%>63 μm) and in the relative and absolute content of ice-rafted detritus (IRD) in the >150- and >500-μm fractions (Fig. 2). The sediments on the inner part of the Vöring plateau are dominantly hemipelagic, and ice rafting is the major source of terrigenous particles during glacials[6]. Our data reveal an increase in IRD per gram of sediment both in the >150- and the >500-μm fractions during stadials, whereas the relative input of particles >63 μm decreases (Fig. 2). This indicates that deposition of coarse material from icebergs was the dominant source of terrigeneous particles during Heinrich events and the smaller events inbetween, and that suspension of finer sediments in meltwater plumes was of minor importance.

Figure 3 shows the typical phase relationship of the signals. The cycles and some of the smaller oscillations culminate in a zone characterized by low foraminifera concentration, an IRD maximum and low $\delta^{18}O$ values (Fig. 3), indicating low salinity and maximum discharge of icebergs into the area. The high rate of iceberg discharge could reflect instability of the ice sheets, when these are at their maximum size, covering large shelf areas and vulnerable to marine drawdown. After the Heinrich events, the SST increases (decreasing *Neogloboquadrina pachyderma* (s.) percentage). This is supported by isotope evidence, as the negative $\delta^{18}O$ spike typically continues through half of the cycle, suggesting a mixed salinity/temperature signal. Compared to the North Atlantic the temperature change is small, demonstrating a large south–north temperature gradient during interstadials. The flux of IRD decreases simultaneously with or shortly after the temperature increase, reflecting a rapid decrease in sediment supply when the ice retreated from the shelf and fewer icebergs drifted over the site. During the next cycle the IRD content increases again, probably because of enhanced sediment supply